Mon. Not. R. Astron. Soc. **000**, 000–000 (0000) Printed 13 January 2017 (MN LATEX style file v2.2)

Bayesian power spectrum estimation at the Epoch of Reionization

L. Lentati[1⋆], P. H. Sims[1,2], C. Carilli[3,1], M. P. Hobson[1], P. Alexander[1], P. Sutter[4,5,6]

[1] *Astrophysics Group, Cavendish Laboratory, JJ Thomson Avenue, Cambridge, CB3 0HE, UK*
[2] *Department of Physics, Brown University, Providence, RI 02912, USA*
[3] *National Radio Astronomy Observatory, Socorro, NM 87801, USA*
[4] *INFN - National Institute for Nuclear Physics, via Valerio 2, I-34127 Trieste, Italy*
[5] *INAF - Osservatorio Astronomico di Trieste, via Tiepolo 11, 1-34143 Trieste, Italy*
[6] *Center for Cosmology and Astro-Particle Physics, Ohio State University, Columbus, OH 43210*

arXiv:1701.03384v1 [astro-ph.IM] 12 Jan 2017

13 January 2017

ABSTRACT

We introduce a new method for performing robust Bayesian estimation of the three-dimensional spatial power spectrum at the Epoch of Reionization (EoR), from interferometric observations. The versatility of this technique allows us to present two approaches. First, when the observations span only a small number of independent spatial frequencies (k-modes) we sample directly from the spherical power spectrum coefficients that describe the EoR signal realisation. Secondly, when the number of k-modes to be included in the model becomes large, we sample from the joint probability density of the spherical power spectrum and the signal coefficients, using Hamiltonian Monte Carlo methods to explore this high dimensional (~ 20000) space efficiently. This approach has been successfully applied to simulated observations that include astrophysically realistic foregrounds in a companion publication. Here we focus on explaining the methodology in detail, and use simple foreground models to both demonstrate its efficacy, and highlight salient features. In particular, we show that including an arbitrary flat spectrum continuum foreground that is 10^8 times greater in power than the EoR signal has no detectable impact on our parameter estimates of the EoR power spectrum recovered from the data.

Key words: methods: data analysis, cosmology: dark ages, reionization, first stars, techniques: interferometric

1 INTRODUCTION

The Epoch of Reionization (EoR) marks a period of history that began approximately 400 Myr after the big bang, when the first ionizing sources formed in an otherwise neutral Universe. For a detailed review of the EoR refer to, for example, Pritchard & Loeb (2012); Loeb & Furlanetto (2013); Morales & Wyithe (2010). In brief, the emergence of these sources resulted in the gradual formation of ionized 'bubbles' in the neutral Hydrogen that made up the surrounding intergalactic medium. These bubbles are thought to have expanded over a redshift range from $z \sim 16 \rightarrow 6$, however the precise timing and duration of the period, as well as the spatial scales on which these bubbles existed as a function of redshift are questions that currently remain largely unanswered.

While recent observations have been able to constrain the bright end of the galaxy luminosity function at low redshifts ($z \lesssim 8$) (Bouwens et al. 2010; Schenker et al. 2013), and other observational programmes have placed constraints on reionization, for example, from the optical depth of Thompson scatering to the CMB (Planck Collaboration et al. 2014), it is thought that the key to answering these questions more completely lies in the detection of the redshifted 21–cm signal from the EoR epoch, which provides a direct link to the density and distribution of the neutral Hydrogen during that time.

This motivation has meant that the detection of the 21–cm signal is one of the major goals for existing, and upcoming low frequency interferometers (e.g the Giant Me-

⋆ E-mail: ltl21@cam.ac.uk

trewave Radio Telescope (GMRT) (Paciga et al. 2013) , the LOw Frequency ARray (LOFAR) (van Haarlem et al. 2013), the Murchison Widefield Array (MWA) (Tingay et al. 2013), the Precision Array to Probe the Epoch of Reionization (PAPER) (Parsons et al. 2014), the Hydrogen Epoch of Reionization Array[1] and the Square Kilometre Array (SKA) (Mellema et al. 2013)) .

In this paper we will, in particular, be concerned with extracting information from the 'late stage' ($z \sim 6 \rightarrow 10$) 21–cm EoR power spectrum obtained using interferometric observations, spatially averaged in either 2 or 3 dimensions to form 'cylindrical' or 'spherical' power spectra respectively.

In recent years, Bayesian methods have become more prevelant in the analysis of interferometric data sets , both in terms of providing optimal imaging techniques (Sutter et al. 2014), and power spectrum analysis in the context of the cosmic microwave background (e.g. Sutter, Wandelt, & Malu (2012); Karakci et al. (2013)).

In the case of the EoR, in order to determine the power spectrum of the fluctuations robustly, one must also account for the presence of Galactic and extragalactic foreground emission (see e.g. Shaver et al. (1999)) which can be orders of magnitude greater than the EoR signal of interest. Typically these foregrounds are dealt with before the estimation of the signal (e.g. Harker et al. 2009; Bonaldi & Brown 2014), but ideally one would fit simultaneously for the EoR signal and the foregrounds in order to account for the covariance between the two correctly, and hence produce an unbiased estimate of the significance of the EoR power spectrum recovered from a given data set.

In this paper we outline a general Bayesian framework that allows just such a joint analysis, which we will consider in two different regimes. First, when the number of spatial scales we wish to include in our model for the EoR power spectrum is small ($\lesssim 20000$) we sample directly from the spherical power spectrum coefficients of the EoR signal. This results in a computational problem that is low–dimensional (~ 10), but high in computational expense, with large dense matrix inversions required in every likelihood calculation. As such, when the number of spatial scales to be included is larger, and the matrix inversions required by the analysis become computationally intractable, we sample instead from the joint probability density of the spherical power spectrum coefficients and the EoR signal realisation. This allows us to eliminate all matrix-matrix multiplications and costly matrix inversions from the likelihood calculation entirely, replacing them with matrix-vector operations and diagonal matrix inversions. In this case the dimensionality is much larger (~ 20000), and so we perform the sampling process using a Guided Hamiltonian Sampler (GHS) (Balan, Ashdown & Hobson, in prep, henceforth B17, see e.g. Lentati et al. (2013) for uses in other astrophysical fields) which exploits Hamiltonian Monte Carlo sampling methods to provide an efficient means of sampling in large numbers of dimensions (potentially $\sim 10^6$). This framework has been applied to simulated interferometric observations that combined realistic astrophysical foregrounds, and the EoR signal in Sims et al. (2016), where it was shown to result in unbiased estimates of the three-dimensional power spectrum of the data sets.

In Sections 2 - 4 we derive the likelihood functions for both these cases. In Section 5 we describe the guided Hamiltonian sampler and how it can be applied to interferometric data analysis. In Section 6 we then apply this framework to a set of simulations to demonstrate the efficacy of the method. These include both high and low signal-to-noise data sets, with and without an additional flat spectrum continuum component. In the latter case we show that this extra continuum component does not affect the power spectrum estimation of the EoR signal present in the data set despite assuming no prior knowledge of the distribution or amplitudes of sources. Finally in Section 7 we offer some concluding remarks.

2 OBSERVING WITH AN INTERFEROMETER

For a generic radio interferometer, the Measurement Equation (Hamaker, Bregman, & Sault 1996; Smirnov 2011) for a pair of antennas p, q observing a single point source allows us to construct a 'visibility matrix', $\mathbf{V_{pq}}$, as:

$$\mathbf{V_{pq}} = \mathbf{J_p B J_q^H}, \tag{1}$$

where $\mathbf{H}$ denotes the Hermitian transpose, $\mathbf{B}$ is the 'brightness matrix', given by

$$\mathbf{B} = \begin{bmatrix} I+Q & U+iV \\ U-iV & I-Q \end{bmatrix}, \tag{2}$$

for Stokes parameters (I, Q, U, V), and $\mathbf{J_{p,q}}$ are 2×2 Jones matrices that describe the cumulative product of all propogation effects along the signal path.

In this work we will be considering only observations that are uncorrupted by (or corrected for), for example, calibration errors, or ionospheric effects. Thus the only contributions to the Jones matrices that we will consider are those that come from a scalar phase delay K_p for each antenna p, defined:

$$K_p = \exp\left(-2\pi i(u_p l + v_p m + w_p(n-1)\right), \tag{3}$$

with l, m, and $n = \sqrt{1-l^2-m^2}$ the direction cosines of the vector from the point source to the antenna, which we denote $\mathbf{\Omega}$, and (u, v, w) the antenna coordinates in wavelengths, and a term that describes the power primary beam of the antenna, which we will denote $\mathbf{P_p}$.

Integrating over the whole sky, we can therefore rewrite Eq. 1 explicitly including only the discussed terms as:

$$\begin{aligned} \mathbf{V_{pq}} &= \int_0^{4\pi} \mathrm{d}\Omega \mathbf{P_p}(\Omega)\mathbf{B}(\Omega)\mathbf{P_q^H}(\Omega) \\ &\times \exp\left(-2\pi i(\mathbf{u_{pq}}\cdot\mathbf{x})\right), \end{aligned} \tag{4}$$

with $\mathbf{x} = (l, m, \sqrt{1-l^2-m^2})$, and $\mathbf{u_{pq}} = (u_p - u_q, v_p - v_q, w_p - w_q)$.

In practice this integral is difficult to evaluate directly, and so we perform a sine projection onto the plane (l, m) at

[1] http://reionization.org

the field centre. If the field of interest is sufficiently small, we can also make the approximation that:

$$\left(\sqrt{1-l^2-m^2}-1\right)w \approx -\frac{1}{2}(l^2+m^2)w \approx 0 \qquad (5)$$

and so consider only $\mathbf{x}=(l,m)$, $\mathbf{u}=(u,v)$. In the context of the simulations presented in Section 6, we consider a primary beam with a full width at half maximum of 8 degrees. For an 8 degree seperation we would have $l^2+m^2 \sim 0.02$, which we consider to be in the regime where this approximation holds, resulting in the expression:

$$\begin{aligned}\mathbf{V_{pq}} &= \int \mathrm{d}^2\boldsymbol{x}\ \mathbf{P_p}(\boldsymbol{x})\mathbf{B}(\boldsymbol{x})\mathbf{P_q^H}(\boldsymbol{x}) \\ &\times \exp\left(-2\pi i(\mathbf{u_{pq}}\cdot\mathbf{x})\right). \end{aligned} \qquad (6)$$

Finally if we consider only the total intensity of the sky $I(\boldsymbol{x})$, we obtain for any pair of antennas (or 'baseline'), operating at a single frequency ν the expression:

$$V_i(\boldsymbol{u_i},\nu_i) = \int \mathrm{d}^2\boldsymbol{x}\ P_i(\boldsymbol{x},\nu_i)I(\boldsymbol{x},\nu_i)\exp(2\pi i\boldsymbol{u_i}\cdot\boldsymbol{x}), \qquad (7)$$

where we have dropped the subscript **pq** for the coordinate vector $\mathbf{u_i}$, and have replaced the visibility matrix with the complex number $V_i(\boldsymbol{u_i},\nu_i)$, and with $P_i(\boldsymbol{x},\nu_i)$ the primary beam profile for baseline i, which we have written explicitly as a function of the observing frequency ν_i.

By the convolution theorm, which states that the Fourier transform of a product of functions is the convolution of the Fourier transforms of the functions seperately, we can define the apeture function $A(\mathbf{u},\nu)$ as the Fourier transform of the primary beam $P(\boldsymbol{x},\nu)$, and the complex visibility plane $S(\boldsymbol{u},\nu)$ as the Fourier transform of the sky brightness $I(\boldsymbol{x},\nu)$, and so rewrite Eq. 7:

$$V_i(\boldsymbol{u_i},\nu_i) = \int \mathrm{d}^2\boldsymbol{u}\ A(\boldsymbol{u}-\boldsymbol{u_i},\nu_i)S(\boldsymbol{u},\nu_i). \qquad (8)$$

In the following sections we now describe our model for $S(\boldsymbol{u},\nu_i)$ that allows us to reconstruct the observed visibilities $V_i(\boldsymbol{u_i},\nu_i)$, while remaining computationally tractable to evaluate.

2.1 Constructing a likelihood

We begin by considering the complex visibilities obtained during an interferometric observation to be the sum of a signal component **s** sampled from the visibility plane, and an instrumental noise component **n**, where we describe the noise as a zero–mean statistically homogeneous Gaussian random field, uncorrelated between different visibilities, with covariance matrix **N** given by:

$$N_{ij} = \left\langle n_i n_j^* \right\rangle = \delta_{ij}\sigma_j \qquad (9)$$

where $\langle..\rangle$ represents the expectation value, and σ_j is the rms value of the noise term for visibility j.

We can therefore write our data vector **d** containing $N_{\rm vis}$ complex visibilities as:

$$\mathbf{d} = \mathbf{s} + \mathbf{n}, \qquad (10)$$

allowing us to construct a general likelihood for a model vector **m** constructed from the set of parameters $\boldsymbol{\Theta}$ as:

$$\begin{aligned}\Pr(\mathbf{d}|\boldsymbol{\Theta}) &= \frac{1}{\sqrt{(2\pi)^{2N_{\rm vis}}\det\mathbf{N}}} \\ &\times \exp\left[-\frac{1}{2}\left(\mathbf{d}-\mathbf{m}(\boldsymbol{\Theta})\right)^T\mathbf{N}^{-1}\left(\mathbf{d}-\mathbf{m}(\boldsymbol{\Theta})\right)\right]\end{aligned} \qquad (11)$$

Henceforth for clarity in the mathematical notation, we will consider our data and hence model vectors to be the concatenation of the real part and imaginary parts, rather than a set of complex values. As such **d**, and **m** will be vectors of length $2\times N_{\rm vis}$, while the diagonal elements of **N** will be given by the rms of the Gaussian noise in the real and imaginary parts of the observed visibilities separately.

2.2 A model grid

In the context of Eq. 8, our model $\mathbf{m}(\boldsymbol{\Theta})$ will be a represention of the complex visibility plane S. In principle we can simply divide the complex plane into equal area cells of side Δu, however clearly our ability to determine the properties of the power spectrum correctly will depend on the number of cells chosen to make up our model. Since both the number of samples required, and the speed of the likelihood evaluation will be strongly dependent upon the number of cells used, a compromise must be made between how accurately our model can represent the true complex plane, and our ability to perform the computational analysis.

In practice a natural maximum size for the model cells exist, as an antenna of diameter D will convolve the complex visibility plane with a function that has scale length $\sim D/2\lambda$. As such, from sampling theory we require $\Delta u < D/2\lambda$ in order for our model to adequately describe the underlying visibility plane.

As we are working with a model grid, initially it may seem a more natural choice to define our model in the image domain. Here we can construct a uniformly spaced $N_{\rm pix}\times N_{\rm pix}\times N_{\rm chan}$ cube, where $N_{\rm pix}$ is the number of pixels along one side of the image, and $N_{\rm chan}$ is the number of channels. Defining the vector of model amplitudes for the pixels in the image as **c**, we can then generate a set of model visibilities **m** as:

$$\mathbf{m} = \mathbf{F_n^{-1}Pc}, \qquad (12)$$

where **P** is a diagonal $N_{\rm pix}\times N_{\rm pix}\times N_{\rm chan}$ matrix that encodes the primary beam correction, and $\mathbf{F_n^{-1}}$ is a $2N_{\rm vis}\times N_{\rm pix}^2 N_{\rm chan}$ matrix, where the factor 2, as previously discussed, accounts for the real and imaginary parts, and describes the inverse Fourier transform from our primary beam corrected image, to the sampled (u,v) coordinates.

As we will show in Section 3, however, when we include a prior on the EoR signal, that prior is defined in k-space, such that contributions to the signal from terms with similar $|k|$ values will be considered to come from a single Gaussian distribution of some variance to be determined during the analysis. When defining the prior in this way, constructing our model in the image domain results in large dense matrix inversions, rapidly making the analysis intractable. If we construct our model in the UV domain instead, this

prior matrix becomes diagonal, and the inversions trivial to compute.

In principle we could replicate the effect of the primary beam in the UV domain by performing a convolution of our model UV grid with the telescope apeture function, the Fourier transform of the primary beam. This, however, is much less computationally tractable than performing a simple multiplication in the image domain, and then performing a Fourier transform of this primary beam corrected image to the UV domain. We can however combine the speed of defining our model in the UV domain with the efficiency of performing the primary beam correction in the image domain by defining a new matrix $\mathbf{P}$, which acts on a vector of model parameters $\mathbf{a}$, which now describes the amplitudes for the real and imaginary parts of the uv–plane such that our model visibilities $\mathbf{m}$ are given by:

$$\begin{aligned} \mathbf{m} &= \bar{\mathbf{F}}\mathbf{a} \\ &= \mathbf{F_n}^{-1}\mathbf{P}\mathbf{F}\mathbf{a} \end{aligned} \tag{13}$$

where the matrix $\mathbf{F}$ is simply the Fourier transform from our gridded (u, v) domain points, to the gridded image. This additional multiplication has no impact on the evaluation time of our likelihood as we can simply precompute the matrix product $\mathbf{F_n}^{-1}\mathbf{P}\mathbf{F}$ and still evaluate the model vector $\mathbf{m}$ in a single matrix–vector multiplication.

2.3 Including large spatial scales

While our definition of the matrix $\mathbf{F}$ in Eq. 13 represents a standard 2–dimensional Fourier transform, this will not correctly model power on spatial scales greater than the size of the image, or equivlantly, on scales such that $|\mathbf{u}| < D/2\lambda$. Linear trends that extend across the image, such as those that can be expected from Galactic foregrounds, will 'leak' into the model coefficients that describe power on scales less than the image size, with $|\mathbf{u}| > D/2\lambda$.

In principle we could incorporate these scales into our model by simply reducing the cell size in our UV model, Δu. For example, power on scales 10 times the size of the image could be incoporated robustly simply by choosing a cell size of $0.1 \times \Delta u$. This however is not computationally tractable, as it will increase the dimensionality of our problem by a factor of 100. In the context of one–dimensional power spectrum recovery from a time series of length T in other fields, van Haasteren et al. (2014) show that using a log spacing for sub-harmonic frequencies ($\nu < 1/T$), and linear spacing for $\nu \geqslant 1/T$ in steps of $\Delta\nu = 1/T$, allows for accurate recovery of the power spectrum when there is significant power in these low frequency terms.

We therefore take an equivalent approach with our two–dimensional analysis. We define a set of 10 evenly log spaced spatial scales between the size of the image, and 10 times the size of the image, and include them in our model, simultaneously with the linear UV domain grid with cell size Δu.

The matrix $\mathbf{F}$ therefore no longer represents the transform from a uniformly gridded UV domain model, to the uniformly gridded image. Instead it defines the transform from our complete gridded UV model, including the points describing power at large spatial scales, to the uniformly gridded image, which remains as in Eq. 13.

2.4 Incomplete UV coverage

In any interferometric observation the coverage of the UV-plane will not be complete. In particular, an interferometer is not sensitive to the (0,0) UV coordinate, as the minimum separation between two antennas cannot be less than the size of the dish, D, so that any observation made will be insensitive to the true mean of the sky. More generally however the sampling of the UV planeby our interferometer will result in gaps, or areas of decreased sensitivity, the precise nature of which will be determined by the arrangement of antennas and length of observation.

We can compute the weighting in the UV–plane that results from the sampling of a set of $N_{\rm vis}$ discrete visibilities, which can also be considered the Fourier transform of the interferometer point spread function. For the current analysis we compute these weights by defining a gridding matrix $\mathbf{G}$ as:

$$\mathbf{G} = \mathbf{F}^{-1}\mathbf{F_n}, \tag{14}$$

where $\mathbf{F_n}$ is a $N_{\rm pix}^2 \times 2N_{\rm vis}$ matrix representing the direct Fourier transform of the visibilities to an $N_{\rm pix} \times N_{\rm pix}$ image domain grid, and $\mathbf{F}^{-1}$ describes the Fourier transform from the gridded image to our gridded uv cells.

In principle UV cells far from the points sampled by the interferometer could have non–zero weights, but would contribute a negligable amount to our model. We therefore compute the weight of any UV cell, W_i, as:

$$W_i = \mathbf{G_i}\mathbf{N}^{-1}\mathbf{G_i}^T, \tag{15}$$

and so we can consider only the $N_{\rm uv}$ cells in our model that contain some fraction of the total weight. For the purposes of this work we take that fraction to be 99%, and include only this subset of cells in the definition of our matrix $\mathbf{F}$.

Working directly in the UV domain it is therefore trivial to account for the incomplete UV coverage of a given observation. For completeness we will discuss briefly one approach to account for this if the model is defined in the image domain, though we will not pursue this approach further as discussed in Section 2.2.

Given a set of $N_{\rm uv}$ UV cells to include in the model, we therefore have a set of $N_{\rm Nuv} \equiv N_{\rm pix}^2 - N_{\rm uv}$ cells that our observation is not sensitive to. By constructing the $N_{\rm pix}^2 \times N_{\rm Nuv}$ matrix $\mathbf{F_{NG}}$ that describes the Fourier transform of those cells to the image grid we can produce a set of basis vectors that describe the null-sky. If we take the SVD of the matrix, which results in three matrices:

$$\mathbf{F_{NG}} = \mathbf{U}\mathbf{S}\mathbf{V}^T, \tag{16}$$

we can take the resultant $N_{\rm pix}^2 \times N_{\rm pix}^2$ matrix $\mathbf{U}$ and separate it into two components:

$$\mathbf{U} = \big(\mathbf{M}, \mathbf{M}_C\big). \tag{17}$$

Here $\mathbf{M}$ is a $N_{\rm pix}^2 \times N_{\rm Nuv}$ matrix, representing the set of

$N_{\rm Nuv}$ orthonormal basis vectors that fully describe the original matrix $\mathbf{F_{NG}}$, while $\mathbf{M}_C$ is the $N_{\rm pix}^2 \times N_{\rm uv}$ complement. This complement can be considered a projection matrix that allows us to take a length $N_{\rm uv}$ vector of parameters, and produce an $N_{\rm pix} \times N_{\rm pix}$ image that contains no contribution from the UV cells that formed our null-sky basis. This is completely analogous to the operation of projecting out unwanted model parameters in other fields, such as pulsar timing (see e.g., van Haasteren & Levin 2013).

2.5 The full K-cube

As mentioned in Section 2.2 we define our EoR signal model directly in (k_x, k_y, k_z) space, using the set of (k_x, k_y) points that correspond to the set of $N_{\rm uv}$ gridded UV coordinates that we include in our analysis as discussed in section 2. These (u, v) coordinates can be translated directly to k_x, k_y coordinates through the relations:

$$\begin{aligned} k_x &= \frac{2\pi u}{D_m} \\ k_y &= \frac{2\pi v}{D_m} \end{aligned} \tag{18}$$

with D_m the transverse comoving distance from the observatory to the redshift of the EoR observation.

Our sampled visibilities, however, are defined in $(\boldsymbol{u}, \nu)$ space and so we must also transform our model cube from k_z to observing frequency ν. We therefore first define the matrix $\mathbf{F}_z$ as

$$F_z(\nu, n_\eta) = \frac{2\nu^2 \kappa_B}{10^{-23} c^2} \frac{\sqrt{2}}{N_{\rm chan}} \sin\left(\frac{2\pi}{B} n_\eta \nu\right), \tag{19}$$

with an equivalent cosine term, B the bandwidth of the observation, and $\eta = n_\eta / B$ the Fourier domain parameter after transforming along the frequency axis, where we include terms up to some maximum $n_\eta = n_{\max\eta}$. The factor $2\nu^2\kappa_B/c^2$ from the Rayleigh-Jeans law, with κ_B the Boltzmann constant, and c the speed of light, at the front of this expression allows us to convert from units of mK in the model (k_x, k_y, k_z) cube, to Janskys (1 Jy = 10^{-26} $\mathrm{Wm^{-2}Hz^{-1}}$). We can then relate η to the cosmological parameter k_z via the relation:

$$k_z = \frac{2\pi H_0 f_{21} E(z)}{c(1+z)^2} \eta, \tag{20}$$

with z the redshift of the EoR observation, H_0 the Hubble constant, $E(z)$ the dimensionless Hubble parameter, f_{21} the frequency of the 21cm line emission, and c the speed of light.

While $\mathbf{F}_z$ represents a typical 1D Fourier transform, the EoR signal present in the data will include fluctuations on scales much longer than the bandwidth of the observation. Written as in Eq. 19 this transform will not correctly account for these low frequencies, causing them to 'leak' into the higher frequency terms included in our model biasing the power spectrum parameter estimates at the scales of interest. In principle these low frequencies could be included simply by adding additional log–spaced Fourier modes to our matrix 19 with $n_\eta < 1$, as in Section 2.3 that using a log spacing for the sub-harmonics allows for accurate recovery of the spectrum when there is significant power in these low frequency terms. In van Haasteren et al. (2014) they note, however, that except for the most extreme cases, these sub-harmonics terms can also be well modelled by a simple quadratic in frequency.

In our model we therefore include a quadratic in frequency to act as a proxy to the sub–harmoinic structure in our data:

$$Q_z = \frac{2\nu_o^2 \kappa_B}{10^{-23} c^2} (q_0 + \nu q_1 + \nu^2 q_2) \equiv \mathbf{Q}_z \boldsymbol{q}, \tag{21}$$

where $\boldsymbol{q} = (q_0, q_1, q_2)$ are amplitude parameters to be fit for.

We can therefore write our final model given the concatenated $N_{\rm uv} \times n_{\max\eta}$ length vector of of signal coefficients $\boldsymbol{a}$, and $N_{\rm uv} \times 3$ quadratic coefficients $\boldsymbol{q}$ defined in the k-cube as:

$$\mathbf{m} = \bar{\mathbf{F}} \left(\mathbf{F}_z \boldsymbol{a} + \mathbf{Q}_z \boldsymbol{q}\right), \tag{22}$$

where $\mathbf{F}_z$ and $\mathbf{Q}_z$ both now represent block diagonal matrices that act independently on each set of coefficients $(\mathbf{a_i}, \mathbf{q_i})$ for each model UV cell i, and $\bar{\mathbf{F}}$ is the two–dimensional primary beam corrected transform described in Eq.13, so that our likelihood at this stage becomes

$$\begin{aligned} \Pr(\mathbf{d}|\boldsymbol{a}, \boldsymbol{q}) &= \frac{1}{\sqrt{(2\pi)^{2N_{\rm vis}} \det \mathbf{N}}} \\ &\times \exp\left[-\frac{1}{2}\left(\mathbf{d} - \bar{\mathbf{F}}\left(\mathbf{F}_z \boldsymbol{a} + \mathbf{Q}_z \boldsymbol{q}\right)\right)^T \right. \\ &\times \left. \mathbf{N}^{-1}\left(\mathbf{d} - \bar{\mathbf{F}}\left(\mathbf{F}_z \boldsymbol{a} + \mathbf{Q}_z \boldsymbol{q}\right)\right)\right]. \end{aligned} \tag{23}$$

2.6 Including foreground models

In order to make a detection of the EoR power spectrum, correctly accounting for foreground signals in the visibilities will be key. These include diffuse emission from the Galaxy, and continuum emission from extragalactic sources (e.g. Jelić et al. 2008), which in combination can be up to five orders of magnitude greater than the EoR signal of interest (Shaver et al. 1999).

In principle, any additional foreground model can be added to the model in Eq 23, either in the image domain, or in the UV. Writing the foreground model as a function of some parameters $\mathbf{m}(\Theta_{\rm fg})$, we would write:

$$\begin{aligned} \Pr(\mathbf{d}|\mathbf{a}, \boldsymbol{\Theta}_{\mathbf{fg}}) &= \frac{1}{\sqrt{(2\pi)^{2N_v} \det \mathbf{N}}} \qquad (24) \\ &\times \exp\left[-\frac{1}{2}\left(\mathbf{d} - \bar{\mathbf{F}}(\mathbf{F}_z \mathbf{a} + \mathbf{Q}_z \boldsymbol{q}) - \mathbf{m}(\Theta_{\rm fg})\right)^T \right. \\ &\times \left. \mathbf{N}^{-1}\left(\mathbf{d} - \bar{\mathbf{F}}(\mathbf{F}_z \mathbf{a} + \mathbf{Q}_z \boldsymbol{q}) - \mathbf{m}(\Theta_{\rm fg})\right)\right], \qquad (25) \end{aligned}$$

and then proceed to sample over the joint parameter space $(\mathbf{a}, \mathbf{q}, \boldsymbol{\Theta}_{\rm fg})$.

One approach advocated to model smooth foreground emission is to use a simple polynomial in frequency (e.g. Bowman, Morales, & Hewitt 2009). In Section 2.5 we note that we include a quadratic in our Fourier transform from frequency to the parameter η in order to model any low

frequency variations that exist in the data that have periods longer than the bandwidth of the observation. We reiterate here, however, that the primary purpose of the quadratic is simply to provide us with an unbiased estimate of the scales of interest (i.e. with $n_\eta \geqslant 1$ in Eq. 19). In principle higher order terms could also be added, however these will be increasingly covariant with the Fourier modes included in the model, and so we do not take this approach.

In section 3 we describe our approach to estimating the EoR power spectrum, incorporating a prior on the signal coefficients $\mathbf{a}$ that incorporates the assumption that the EoR signal is spatially homogenous. We do not, however, incorporate such a prior on the quadratic terms in our estimation of the power spectrum, as these terms will likely be dominated by foreground emission and so will not have the same homogeneity, at least in the case of the Galactic foreground. While in principle a separate Gaussian prior could be included for these quadratic terms, in order to make our analysis of the EoR signal more conservative we use a less informative uniform prior on the amplitudes of these coefficients.

In our simulations in Section 6 we will be considering only simple continuum models, with flat spectrum sources, however a more detailed account on the effect of foregrounds, when including realistic frequency evolution and spatial structure, using the technique described in this work is given in Sims et al. (2016).

3 ESTIMATING THE POWER SPECTRUM

Assuming the EoR signal to be spatially homogenous the covariance matrix $\mathbf{\Phi}$ of the k-space coefficients $\boldsymbol{a}$ will be diagonal, with components

$$\Phi_{ij} = \langle a_i a_j \rangle = \varphi_i \delta_{ij}, \tag{26}$$

where there is no sum over i, and the set of coefficients φ_i represent the theoretical power spectrum for the EoR signal.

In the framework we will describe below we are free to choose any functional form for the coefficients φ_i. It is here then that, should one wish to fit a specific model to the power spectrum at the point of sampling, to perform model selection for example, the set of coefficients φ_i should be given by some function $f(\Theta)$, where we sample from the parameters Θ from which the power spectrum coefficients φ_i can then be derived.

In Section 6 we will be comparing the results of our method with an input simulation obtained using the seminumerical 21cm FAST algorithm (Mesinger, Furlanetto, & Cen 2011; Mesinger & Furlanetto 2007). After computing the EoR simulation, 21cm FAST outputs a spherical power spectrum of the simulated cube, performing a 3–dimensional FFT and averaging all the Fourier coefficients that fall within some spherical shell in k-space in order to calculate the power spectrum within that bin.

In order to draw the most direct comparison with the input simulation, we therefore calculate the quantity $|k| = \sqrt{k_x^2 + k_y^2 + k_z^2}$ for each k–space coefficient $\mathbf{a}$ in our model, and define a set of bins in the quantity $|k|$. As in 21cm FAST, we define the edges of these bins to be spaced as $1.5^n \Delta |k|$ for bins $n = 1 \ldots n_{\rm max}$ with $n_{\rm max}$ the largest bin included in the model. Our model for the power spectrum φ will then be a set of independent parameters φ_i, one for each $|k|$ bin i.

We then write the joint probability density of the model coefficients that define our power spectrum, and the k-space signal coefficients $\Pr(\boldsymbol{\varphi}, \mathbf{a} \mid \mathbf{d})$ as:

$$\Pr(\boldsymbol{\varphi}, \mathbf{a}, \mathbf{q} \mid \mathbf{d}) \propto \Pr(\mathbf{d}|\mathbf{q}, \mathbf{a}) \Pr(\mathbf{a}|\boldsymbol{\varphi}) \Pr(\boldsymbol{\varphi}) \Pr(\boldsymbol{q}) \tag{27}$$

and then marginalise over all $\mathbf{a}$ and $\mathbf{q}$ in order to find the posterior for the parameters that define the power spectrum $\boldsymbol{\varphi}$ alone.

For our choice of $\Pr(\boldsymbol{\varphi})$ we use either a uniform prior in the amplitude of the coefficient, or a uniform prior in $\log_{10}$ space. The latter case is the least informative prior we can choose, however when the goal is to set an upper limit a prior that is uniform in log space is not appropriate, as the upper limit is dependent upon the bounds of the prior. When this is the case we use a prior that is uniform in the amplitude. In either case we draw our samples from the parameter ρ_i, such that:

$$\varphi_i = \frac{2\pi^2 N_{\rm pix}^2 N_{\rm chan} \Omega_{\rm pix}^4}{|\boldsymbol{k}|_i^3 V} 10^{\rho_i}, \tag{28}$$

with V the surveyed volume in Mpc^3, and $\Omega_{\rm pix}$ the image pixel size in radians, and the spherical power spectrum coefficients 10^{ρ_i} defined in units of mK^2 $(\mathrm{h}^{-1}\ \mathrm{Mpc})^3$.

Given these two choices of prior, and assuming a uniform prior on the quadraditc amplitude parameters $\mathbf{q}$ such that $\Pr(\boldsymbol{q}) = 1$, the conditional distribution $\Pr(\mathbf{d}|\mathbf{q}, \mathbf{a})$ remains as in Eq. 23, while the latter part of Eqn 27 is given by:

$$\Pr(\mathbf{a}|\rho)\Pr(\boldsymbol{\rho}) \propto \frac{1}{\sqrt{\det \varphi}} \exp\left[-\mathbf{a}^{*T} \mathbf{\Phi}^{-1} \mathbf{a}\right]. \tag{29}$$

when assuming a log-uniform prior on the amplitude of the power spectrum coefficients ($\Pr(\boldsymbol{\rho}) = 1$), and when using a prior that is uniform in the amplitude:

$$\Pr(\mathbf{a}|\rho)\Pr(\boldsymbol{\rho}) \propto \frac{1}{\sqrt{\det \varphi}} \exp\left[-\mathbf{a}^{*T} \mathbf{\Phi}^{-1} \mathbf{a}\right] \prod_{s=1}^{N_s} 10^{\rho_s}, \tag{30}$$

with N_s the number of spherical power spectrum bins used in the prior.

3.1 A non-Gaussian prior

The approach outlined in Section 3 explicitly assumes that the signal coefficients that fall into a specific $|k|$ bin are well described by a Gaussian random process, however if desired we can relax this assumption and use a non-Gaussian prior instead. We use the approach developed in Rocha et al. (2001), which is based on the energy eigenmode wavefunctions of a simple harmonic oscillator, and has since been applied to other areas of astrophysics (Lentati, Hobson, & Alexander 2014), which we outline in brief below.

For a general random variable x, we write the PDF for fluctuations in x as:

$$\Pr(x|\sigma, \boldsymbol{\alpha}) = \exp\left[-\frac{x^2}{2\sigma^2}\right] \left| \sum_{n=0}^{\infty} \alpha_n C_n H_n\left(\frac{x}{\sqrt{2}\sigma}\right) \right|^2 \tag{31}$$

with α_n free parameters that describe the relative contributions of each term to the sum, and

$$C_n(\sigma) = \frac{1}{(2^n n! \sqrt{2\pi}\sigma)^{1/2}}, \tag{32}$$

is a normalization factor. Equation 31 forms a complete set of PDFs, normalised such that:

$$\int_{-\infty}^{\infty} \mathrm{d}x \, \exp\left[-\frac{x^2}{\sigma^2}\right] C_n H_n\left(\frac{x}{\sqrt{2}\sigma}\right) C_m H_m\left(\frac{x}{\sqrt{2}\sigma}\right) = \delta_{mn}, \tag{33}$$

with δ_{mn} the Kronecker delta, where the ground state, H_0, reproduces a standard Gaussian PDF, and any non-Gaussianity in the distribution of x will be reflected in non-zero values for the coefficients α_n associated with higher order states.

The only constraint we must place on the values of the amplitudes $\boldsymbol{\alpha}$ is:

$$\sum_{n=0}^{n_{\max}} |\alpha_n|^2 = 1 \tag{34}$$

with $n_{\max}$ the maximum number of coefficients to be included in the model for the PDF. This is performed most simply by setting:

$$\alpha_0 = \sqrt{1 - \sum_{n=1}^{n_{\max}} |\alpha_n|^2}. \tag{35}$$

Using this formalism we can then parameterise any non-Gaussianity in the coefficients $\mathbf{a}$ by rewriting Eq. 29:

$$\begin{aligned} \Pr(\mathbf{a} \mid \boldsymbol{\varphi}, \alpha) &= \exp\left[-\frac{1}{2}\mathbf{a}^T \boldsymbol{\Phi}^{-1} \mathbf{a}\right] \\ &\times \prod_{i=1}^{n} \left| \sum_{n=0}^{n_{\max}} \alpha_n C_n(\varphi_i) H_n\left(\frac{a_i}{\sqrt{2\varphi_i}}\right) \right|^2 . \end{aligned} \tag{36}$$

The advantage of this method is that one may use a finite set of non-zero α_n to model the non-Gaussianity, without mathematical inconsistency. Any truncation of the series still yields a proper distribution, in contrast to the more commonly used Edgeworth expansion (e.g. Contaldi et al. 2000).

3.2 Performing the sampling

How we now perform the sampling depends entirely on the size of the k-cube we will be using to describe the EoR signal present in the visibilities. When the size of the k-cube, and thus the number of signal parameters used to describe the signal is small (< 20000), we can marginalise over the coefficients $\mathbf{a}$ analytically and sample directly from the power spectrum coefficients $\boldsymbol{\rho}$, a process we describe in Section 4. In this scenario we can perform the sampling using MultiNest (Feroz & Hobson 2008; Feroz, Hobson, & Bridges 2009), allowing us to perform robust evidence evaluation, and perform model selection on the EoR power spectrum.

If however we wish to sample over a larger number of signal coefficients, the matrix to be inverted when performing the marginalisation analytically will become too large to make this approach computationally tractable. In this situation we can perform the marginalisation numerically, sampling directly from the high dimension, joint probability distribution described in Eq 27, a process made possible through the use of a GHS (B17) which we describe in the Section 5.

4 THE SMALL K-CUBE REGIME: ANALYTICAL MARGINALISATION OVER THE SIGNAL COEFFICIENTS

In order to perform the marginalisation over the signal coefficients $\mathbf{a}$ and $\mathbf{q}$, we first simplify our notation by defining the vector $\mathbf{b}$ as the concatenation of the vectors $\mathbf{a}$ and $\mathbf{q}$, and the matrix $\mathbf{T}$ such that our signal can be rewritten:

$$\mathbf{m} = \bar{\mathbf{F}}\left(\mathbf{F}_z \boldsymbol{a} + \mathbf{Q}_z \boldsymbol{q}\right) = \mathbf{T}\mathbf{b}. \tag{37}$$

We then write the log of the likelihood in Eq 27, which denoting $\mathbf{T}^T\mathbf{N}^{-1}\mathbf{T} + \boldsymbol{\Phi}^{-1}$ as $\boldsymbol{\Sigma}$, where the elements of the matrix $\boldsymbol{\Phi}^{-1}$ that correspond to the coefficients $\boldsymbol{q}$ are set to zero, and denoting $\mathbf{T}^T\mathbf{N}^{-1}\mathbf{d}$ as $\bar{\mathbf{d}}$ is given by:

$$\log \mathrm{L} = -\frac{1}{2}\mathbf{d}^T\mathbf{T}^T\mathbf{N}^{-1}\mathbf{T}\mathbf{d} - \frac{1}{2}\mathbf{b}^T\boldsymbol{\Sigma}\mathbf{b} + \bar{\mathbf{d}}^T\mathbf{b}. \tag{38}$$

Taking the derivitive of $\log \mathrm{L}$ with respect to $\mathbf{a}$ gives us:

$$\frac{\partial \log \mathrm{L}}{\partial \mathbf{b}} = -\boldsymbol{\Sigma}\mathbf{b} + \bar{\mathbf{d}}^T, \tag{39}$$

which can be solved to give us the maximum likelihood vector of coefficients $\hat{\mathbf{b}}$:

$$\hat{\mathbf{b}} = \boldsymbol{\Sigma}^{-1}\bar{\mathbf{d}}. \tag{40}$$

Re-expressing Eq. 38 in terms of $\hat{\mathbf{b}}$:

$$\begin{aligned} \log \mathrm{L} &= -\frac{1}{2}\mathbf{d}^T\mathbf{T}^T\mathbf{N}^{-1}\mathbf{T}\mathbf{d} + \frac{1}{2}\hat{\mathbf{b}}^T\boldsymbol{\Sigma}\hat{\mathbf{b}} \\ &- \frac{1}{2}(\mathbf{b}-\hat{\mathbf{b}})^T\boldsymbol{\Sigma}(\mathbf{b}-\hat{\mathbf{b}}), \end{aligned} \tag{41}$$

the 3rd term in this expression can then be integrated with respect to the m elements in $\mathbf{b}$ to give:

$$\begin{aligned} I &= \int_{-\infty}^{+\infty} \mathrm{d}\mathbf{b} \exp\left[-\frac{1}{2}(\mathbf{b}-\hat{\mathbf{b}})^T\boldsymbol{\Sigma}(\mathbf{b}-\hat{\mathbf{b}})\right] \\ &= (2\pi)^m \det \boldsymbol{\Sigma}^{-\frac{1}{2}}. \end{aligned} \tag{42}$$

Our marginalised probability distribution for a set of EoR power spectrum coefficients is then given as:

$$\begin{aligned} \Pr(\varphi \mid \mathbf{d}) &\propto \frac{\det(\boldsymbol{\Sigma})^{-\frac{1}{2}}}{\sqrt{\det(\varphi)\ \det(\mathbf{N})}} \\ &\times \exp\left[-\frac{1}{2}\left(\mathbf{d}^T\mathbf{N}^{-1}\mathbf{d} - \bar{\mathbf{d}}^T\boldsymbol{\Sigma}^{-1}\bar{\mathbf{d}}\right)\right]. \end{aligned} \tag{43}$$

When taking this approach in Section 6 we use the MAGMA (Matrix Algebra on GPU and Multicore Architectures) GPU accelerated linear algebra package[2] to perform the cholesky decomposition for each likelihood evaluation.

[2] http://icl.cs.utk.edu/magma/

5 THE LARGE K-CUBE REGIME: NUMERICAL MARGINALISATION OVER THE SIGNAL COEFFICIENTS

For a detailed account of both Hamiltonian Monte Carlo (HMC) and GHS refer to B17 or Lentati et al. (2013), here we will provide only a brief introduction of the key aspects of each.

HMC sampling (Duane et al. 1987) has been widely applied in Bayesian computation (Neal, R 1993), and has been successfully applied to problems with extremely large numbers of dimensions ($\sim 10^6$ see e.g. Taylor, Ashdown, & Hobson (2008)). Where conventional MCMC methods move through the parameter space by a random walk and therefore require a prohibitive number of samples to explore-high dimensional spaces, HMC exploits techniques that describe the motion of particles in potential wells, and suppresses this random walk behaviour. This allows the HMC approach to maintain a reasonable efficiency even for high-dimensional problems.

Possibly the main shortcoming of traditional HMC methods is that it requires a large number of tuning parameters in order to navigate the parameter space. In particular, every parameter requires a step size, and the total number of steps in each iteration of the sampler must also be chosen. These are typically determined via expensive tuning runs. The GHS is designed to bypass much of this tuning by using the Hessian of the sampled probability distribution, calculated at its peak, to set the step size and covariance of the parameter space. The number of steps at each iteration is then drawn from a uniform distribution U(1, nmax), with nmax of ten found to be suitable for all tested problems. A single global scaling parameter for the step size is then the only tunable parameter, chosen such that the acceptance rate for the GHS is ∼68%.

Therefore in order to perform sampling we need the following:

- The gradient of Ψ for each parameter x_i
- The peak of the joint distribution
- The Hessian at that peak

The gradients of our parameters are given by the following:

$$\frac{\partial \Psi}{\partial \mathbf{b}} = -(\mathbf{d} - \mathbf{T}\mathbf{b})^T \mathbf{N}^{-1}\mathbf{T} + \mathbf{b}^T \mathbf{\Phi}^{-1} \tag{44}$$

$$\frac{\partial \Psi}{\partial \rho_i} = \frac{1}{2}\mathrm{Tr}\left(\mathbf{\Phi}^{-1}\frac{\partial \mathbf{\Phi}}{\partial \rho_i}\right) - \frac{1}{2}\mathbf{b}^T\mathbf{\Phi}^{-1}\frac{\partial \mathbf{\Phi}}{\partial \rho_i}\mathbf{\Phi}^{-1}\mathbf{b} \tag{45}$$

and the components of the Hessian are:

$$\frac{\partial^2 \Psi}{\partial \mathbf{b}^2} = \mathbf{T}^T\mathbf{N}^{-1}\mathbf{T} + \mathbf{\Phi}^{-1} \tag{46}$$

$$\frac{\partial^2 \Psi}{\partial \rho_i^2} = \mathbf{b}^T\mathbf{\Phi}^{-1}\frac{\partial \mathbf{\Phi}}{\partial \rho_i}\mathbf{\Phi}^{-1}\frac{\partial \mathbf{\Phi}}{\partial \rho_i}\mathbf{\Phi}^{-1}\mathbf{b} - \frac{1}{2}\mathbf{b}^T\mathbf{\Phi}^{-1}\frac{\partial^2 \mathbf{\Phi}}{\partial \rho_i^2}\mathbf{\Phi}^{-1}\mathbf{b} \tag{47}$$

$$\frac{\partial^2 \Psi}{\partial \rho_i \partial \mathbf{b}} = -\mathbf{\Phi}^{-1}\frac{\partial \mathbf{\Phi}}{\partial \rho_i}\mathbf{\Phi}^{-1}\mathbf{b} \tag{48}$$

For a set of power spectrum coefficients ρ we can solve for the maximum set of signal coefficients $\mathbf{b}_{\rm max}$ analytically using Eq. 40 so when searching for the global maximum we need only search over the subset of parameters ρ. This is achieved by using either a particle swarm algorithm (Kennedy (1995, 2001) and for uses in cosmological parameter estimation see e.g. Prasad & Souradeep (2012)) or using a gradient search optimization Gilbert & Lemarchal (1989).

5.1 Low signal-to-noise parameterisation

In Lentati et al. (2016) an alternative parameterisation of the likelihood described in Eq. 29 is described that is much more efficient in the low signal-to-noise regime, where the power spectrum coefficients are not detected. We can anticipate that, at least at first, this is likely to be the case with the EoR signal, and thus we summarise this new parameterisation in the context of our three-dimensional power spectrum analysis below.

Rather than sample from the parameters $\mathbf{a}$, we instead sample from the related parameters $\mathbf{u}$ where for the ith signal amplitude we will have:

$$a_i = u_i\sqrt{\varphi_i}, \tag{49}$$

where as before φ_i is the three-dimensional power spectrum coefficient that describes the standard deviation of the ith amplitude parameter. In order to still sample uniformly in the original parameters, $\mathbf{a}$, we then include an additional term, the determinant of the Jacobian describing the transformation from a_i to u_i. The Jacobian in this case has elements:

$$J_{i,j} = \sqrt{\varphi_i}\delta_{i,j,}, \tag{50}$$

with $\delta_{i,j,}$ the kroneckar delta. The determinant is therefore:

$$\det(\mathbf{J}) = \prod_{i=0}^{m}\sqrt{\varphi_i}, \tag{51}$$

which acts to cancel exactly with the determinant of the matrix $\mathbf{\Psi}$ in Eq. 29. In the following work when using the GHS we will use both parameterisations dependent upon whether we are in the high or low signal-to-noise regime.

6 APPLICATION TO SIMULATIONS

We now apply the methods described in the preceding sections to a series of five simulations. In the first three of these we perform the simulation using a 37 element interferometer, with antenna locations shown in Fig. 1 (top, left), while for the final two simulations we use a 61 element array (Fig. 1 bottom, left). In both cases we simulate 38 2KHz channels spanning the range 122.17∼129.90MHz and take our antennas configuration to be representative of the upcoming HERA 37 and 61 element arrays.

We calculate the theoretical instrumental thermal noise for our simulation per unit time τ given the parameters in Table 1, as in Taylor, Carilli, & Perley (1999):

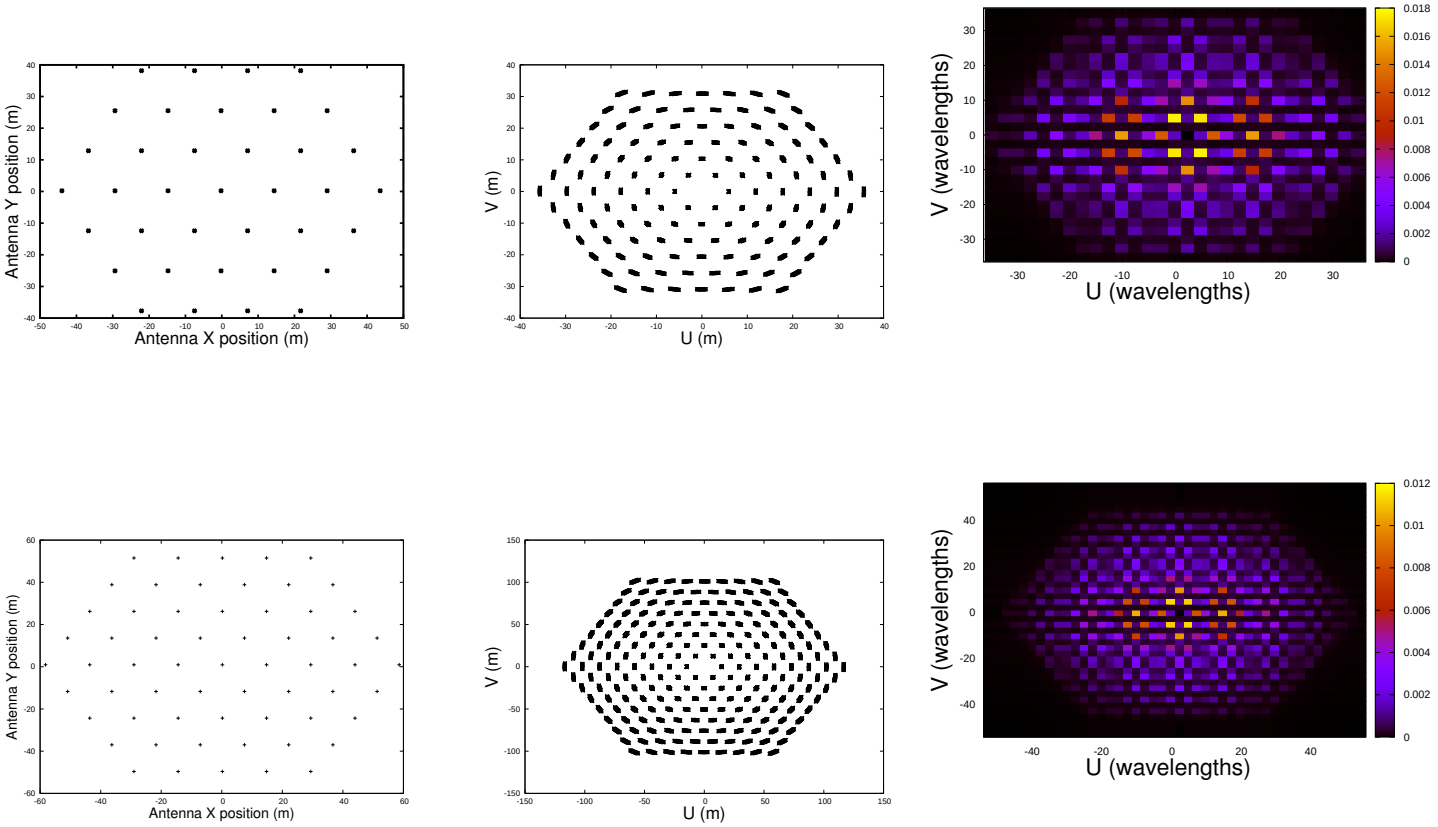

Figure 1. [Top] (Left) Antenna positions for the 37 element interferometer used in simulations 1-3 in Section 6. (Middle) Sampled (u, v) coordinates from a 30 minute observation, and (Right) the relative weights of the (u, v) obtained from Eq. 15 normalised to have a sum of 1. [Bottom] As [Top] but for the 61 element array used in simulations 4-5 in Section 6.

Parameter	Description	Value
η_s	System efficiency	1
$\Delta\nu$	Bandpass of observation	200 kHz
η_a	Antenna efficiency	1
A	Antenna effective area	150 m^2
$T_{\rm sys}$	System temperature	550 K

Table 1. Instrument and observation parameters used to calculate the variance of the theoretical instrumental thermal noise per unit time τ.

$$\sigma(\tau) = 10^{-26}\frac{1}{\eta_{\rm s}}\frac{2k_bT_{\rm sys}}{\eta_{\rm a}A}\frac{1}{\sqrt{2\Delta\nu\tau}} \qquad (52)$$

For each simulation we use the array configurations for the 37 or 61 element interferometers in Fig.1 as input to the CASA[3] (Common Astronomy Software Applications) simobserve tool, to obtain the set of observed (u, v) coordinates that correspond to a series of 30 second integrations over a single 30 minute pointing given those configurations. We take the pointing centre to have right ascension equal to 0.0, and declination equal to -30.0. This results in 21870 sampled (u, v) coordinates per channel for the 37 element array, and 58141 per channel for the 61 element array (Fig. 1, middle, top and bottom panels respectively).

Our input sky models are constructed using 2048×2048 pixel channels, with a resolution of $\sim$ 40 arcseconds per pixel, giving a total field of view of $\sim 23 \times 23$ degrees. We then multiply these sky models by a Gaussian primary beam with a full width at half max of 8 degrees at 122.17 MHz, and evaluate the direct Fourier transform of the observed sky-models onto the sampled (u, v) points obtained previously.

We now describe each of the five simulations in more detail below:

Simulation 1

A 2000 hrs simulation of a single flat spectrum point source 10.4 degrees away from the primary beam center, resulting in a 1000σ detection using the 37 element array shown in Fig. 1 (top). We include uncorrelated thermal noise in each visibility. To simulate 4000 repetitions of our 30 minute observation we therefore add 0.045Jy noise to

[3] http://casa.nrao.edu

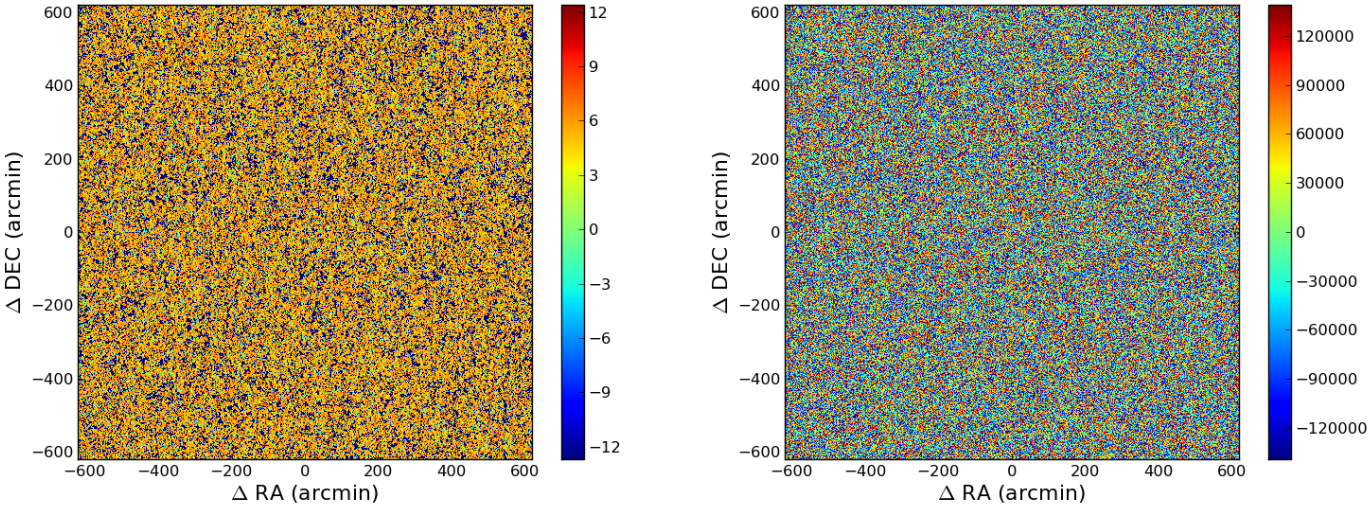

Figure 2. (left) A single channel from simulation of the EoR signal using the seminumerical 21cm FAST algorithm (Mesinger, Furlanetto, & Cen 2011; Mesinger & Furlanetto 2007) described in section 6, after subtracting the mean in the spatial variations for that channel. (right) A single channel from a simple continuum sky simulation described in section 6, after subtracting the mean in the spatial variations for that channel. The continuum simulation is scaled such that the power is a factor 10^8 greater than in the EoR simulation. In both cases the colour scale is in mK.

each of the 21870 visibilities in each channel. In order to compare equivalent simulations we use the same white noise realization for simulations 1-3, and for simulations 4-5. For ease of interpretation we do not include the quadratic described in Eq. 21 in our model when analysing this simulation. The purpose of this first simulation is to show in a straightforward way how our approach automatically accounts for the frequency dependence of the UV-sampling, which causes observed low frequency structure along individual baselines.

Simulation 2
A 160 hour integration including only the EoR signal and the uncorrelated thermal noise described in Simulation 1. We generate the EoR signal using the seminumerical 21cm FAST algorithm (Mesinger, Furlanetto, & Cen 2011; Mesinger & Furlanetto 2007) to simulate a cosmological volume of 1024^3 Mpc^3. We use this same EoR realisation in all subsequent simulations. An example of one channel from this EoR simulation is shown in Fig. 2 (left).

Simulation 3
As Simulation 2, but an additional flat spectrum continuum component is added to the model, shown in Fig. 2 (right). Each pixel in the continuum model is assigned a random positive value drawn uniformly between zero and one, which is then held constant across the 38 channels for that pixel. We then scale the image so that the total power in the mean subtracted continuum is $\sim 10^8$ times that of the EoR signal. An example of one channel from this continuum simulation is shown in Fig. 2 (right).

Simulation 4
As Simulation 2, however we use the 61 element array shown in Fig. 1 (bottom).

Simulation 5
As Simulation 4, but an additional flat spectrum continuum component is added to the model as described in Simulation 3.

In order to adequately sample the aperture function of the Gaussian primary beam in the UV plane, we define our UV cells to each have a width of 2.5λ. We then use Eq. 15 to determine the set of cells to include in our model. The weights for each cell are shown in Fig. 1 (right) for the 37 and 61 element arrays (top and bottom panels respectively). Including all cells that contribute up to 99% of the total weight, we find results in 650, and 1142 UV cells per η mode included in the model for the 37 and 61 element arrays respectively.

For simulations 1-3 we will use the analytic marginalisation over the signal coefficients described in Section 4, sampling from the 7 dimensional s pherical power spectrum using the MultiNest algorithm. For simulations 4-5 the number of signal coefficients included in the model is too great for this analytic approach, and so we perform this marginalisation numerically using the GHS described in Section 5.

6.1 Results for Simulation 1

In Figure 3 (red lines) we show the injected real (left) and imaginary (right) signal for the longest (top) and shortest (bottom) baselines for simulation 1, containing a single point source observed by the 37 element array shown in Fig. 1 (top). Noticeably the baselines show structure as a function of frequency despite the fact that the injected source has a flat spectrum. This is simply a result of the baselines sam-

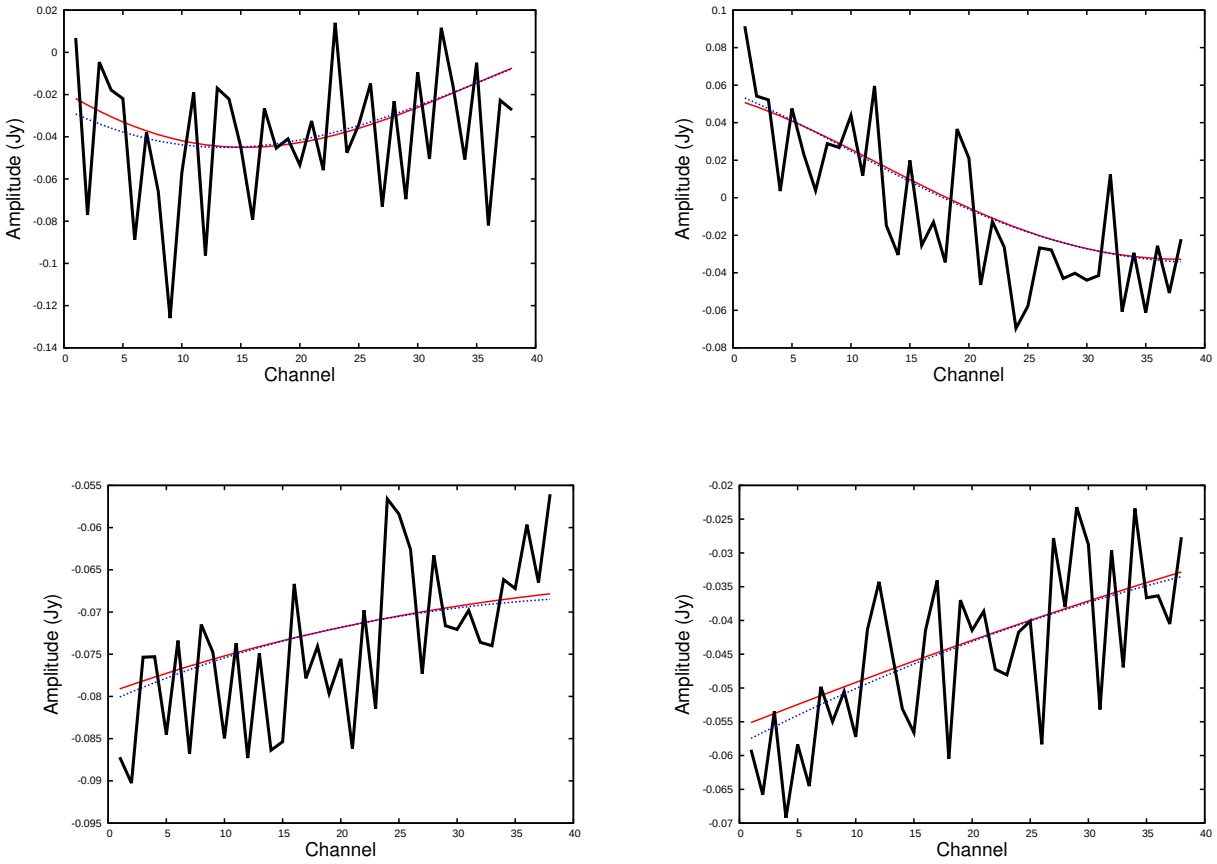

Figure 3. The real (left) and imaginary (right) components from the longest (top) and shortest (bottom) baselines taken from simulation 1. The red line in each case is the injected data, the black line is the injected data with added uncorrelated noise, and the blue line is the maximum likelihood recovered signal from our analysis for the offset term in our model. This simulation contains a single flat spectrum point source, however as each baseline samples a range of different (u, v) coordinates as a function of frequency it is seen to have structure. We note here that we did not include the quadratic described in Eq.21 in our model for this simulation, the recovered structure comes solely as a result of projecting our model k-cube onto the sampled visibility points.

pling a range of UV coordinates, and therefore signal phase, as a function of frequency. For this simulation we have not included the linear or quadratic terms in our model, opting to use only the offset, and the set of the 18 lowest frequency Fourier modes. The structure recovered from our analysis (blue lines) is plotted only for the offset term from this model for the maximum likelihood solution. In all cases this is completely consistent with the injected data, within the level of the added noise.

In Table 2 we list the Evidence values for models that include different sets of power spectrum coefficients, where those power spectrum coefficients not listed for each model have been set to 0. This allows us to address the question of model selection in a Bayesian framework. In particular we can use the difference in the log Evidence $\mathcal{Z}$ between two competing models, which we will denote $\Delta\mathcal{Z} = \mathcal{Z}_1 - \mathcal{Z}_2$, to obtain the probability that the data supports model 1 over model 2 as:

$$P = \frac{\exp \Delta\mathcal{Z}}{1 + \exp \Delta\mathcal{Z}}. \quad (53)$$

Table 2. log Evidence values for Simulation 1

Model Coefficients	log Evidence
0	0.0
ρ_1	-0.3
ρ_2	-0.2
ρ_3	-0.5
ρ_4	0.0
ρ_5	-0.3
ρ_6	0.8
ρ_7	-0.3

In the following we will consider $\Delta\mathcal{Z} > 3$ to be significant evidence in favour of including a particular power spectrum coefficient in the model, however for more detail on the use of the Evidence in model selection refer to, e.g. Kass & Raftery (1995). Given this threshold, we can see none of the power spectrum coefficients result in a significant increase in the Evidence, indicating that the included offset term is sufficient to model the entire signal present in the data,

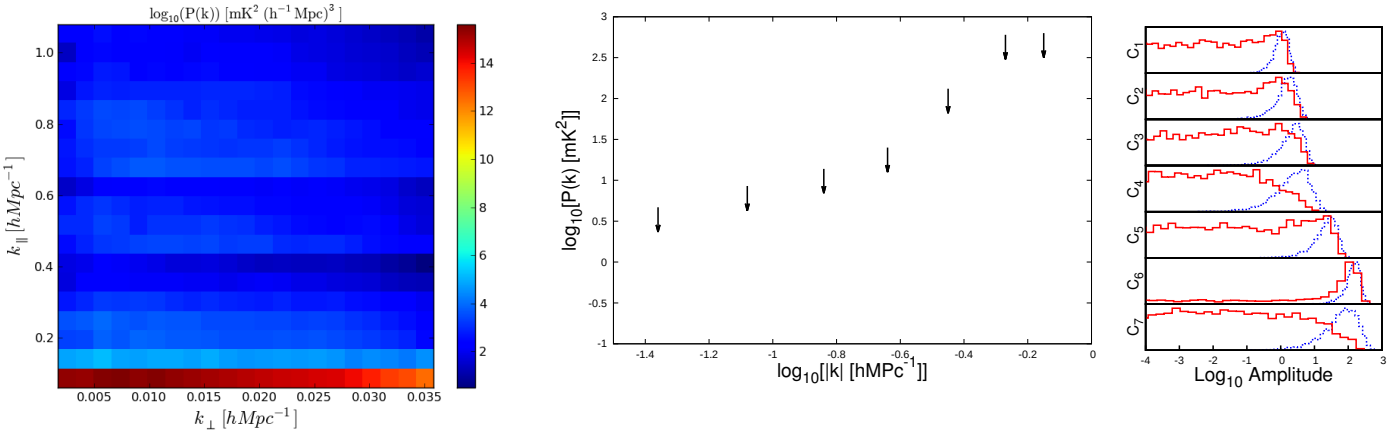

Figure 4. (Left) Maximum likelihood reconstructed cylindrical power spectrum for simulation 1 containing a single point source. There is only significant power present in the lowest k-mode corresponding to the offset term in our model k-cube. (Right) One dimensional marginalised posteriors for the 7 spherical power spectrum coefficients from Simulation 1 using priors that are uniform in the amplitude (blue lines) and uniform in the log of the amplitude (red lines). No significant power is detected in any of the coefficients, indicating that all the power in the simulation is correctly modelled by the offset term in the k-cube.

Table 3. log Evidence values for Simulations 2-3

Model Coefficients	Sim 1 log Evidence	Sim 2 log Evidence
0	0.0	0.0
ρ_2	30.2	30.0
ρ_2, ρ_3	35.9	36.0
ρ_2, ρ_3, ρ_4	37.1	37.3

simply as a result of defining our model cube in wavelengths, and then projecting this onto our sampled data points.

In Figure 4 we show the 1 dimensional marginalised posterior parameter estimates for the 7 spherical power spectrum coefficients when included simultaneously in the model. All coefficients are consistent with zero, consistent with the change in the Evidence when considering each term individually We note here that the most significant increase in the Evidence came from including ρ_6, and from Figure 4 we can see the posterior for the 6th coefficient shows a marginal probability of there being power in the data set at that scale. This same feature is present at similar significance in simulations 2-3 however, which use the same thermal noise realisation, implying that this is simply a fluctuation in the uncorrelated noise.

6.2 Results for Simulations 2-3

As for Simulation 1, Table 3 lists the Evidence for models that include different sets of power spectrum coefficients for simulations 2 and 3. In this case as we increase the number of coefficients in the model, we only list the particular set that maximises the Evidence. We find that the Evidence values are consistent between simulations 1 and 2, and conclude that only 2 spherical power spectrum coefficients have been detected with significance above our threshold. Figure 4 shows the results from the analysis of Simulations 2 and 3 using the analytic marginalisation process described in Section 4 when including all 7 spherical power spectrum coefficients simultaneously in the model. In particular, we show the one dimensional marginalised posteriors for the spherical power spectrum coefficients from simulations 2 (middle plot) and 3 (right plot) when using priors that are uniform in the amplitude of the coefficient (blue line) and uniform in the log of the amplitude (red line). We indicate the 2 coefficients that we consider to be detections in Fig. 4 (left) as the points with uncertainties, whilst the remaining five amplitudes are taken to be 2σ upper limits obtained using the prior that is uniform in the amplitude of the coefficient and are represented as arrows in this plot. All the coefficients for both simulations are consistent with the values obtained from the input cube within 2σ uncertainties. Critically, the results from both simulations are completely consistent with one another, indicating that the addition of a significant flat spectrum continuum component, with power 8 orders of magnitude greater than the EoR signal, did not impact our ability to correctly infer the properties of the power spectrum.

Of note is that, compared to simulation 1, the upper limit for the lowest spherical power spectrum bin is considerably worse, despite the fact that the thermal noise realisation is exactly the same between these sets of simulations. That is because for these two (and subsequent) simulations, we are including the quadratic in our model as a proxy to the low frequency fluctuations as a function of frequency. The quadratic is most strongly correlated with the lowest frequency, and so decreases our sensitivity to terms in that lowest k-bin. Including higher order polynomial terms in the fit will push this effect into the higher k-bins, as cubics, or beyond, will be more strongly correlated with the higher frequency modes in the model. We stress however that this is not a shortcoming of our analysis method. Fully incorporating the covariance between the low-frequency terms, assumed to be dominated by foregrounds, and the higher-frequency modes of interest is critical in order to obtain unbiased estimates of the EoR power spectrum.

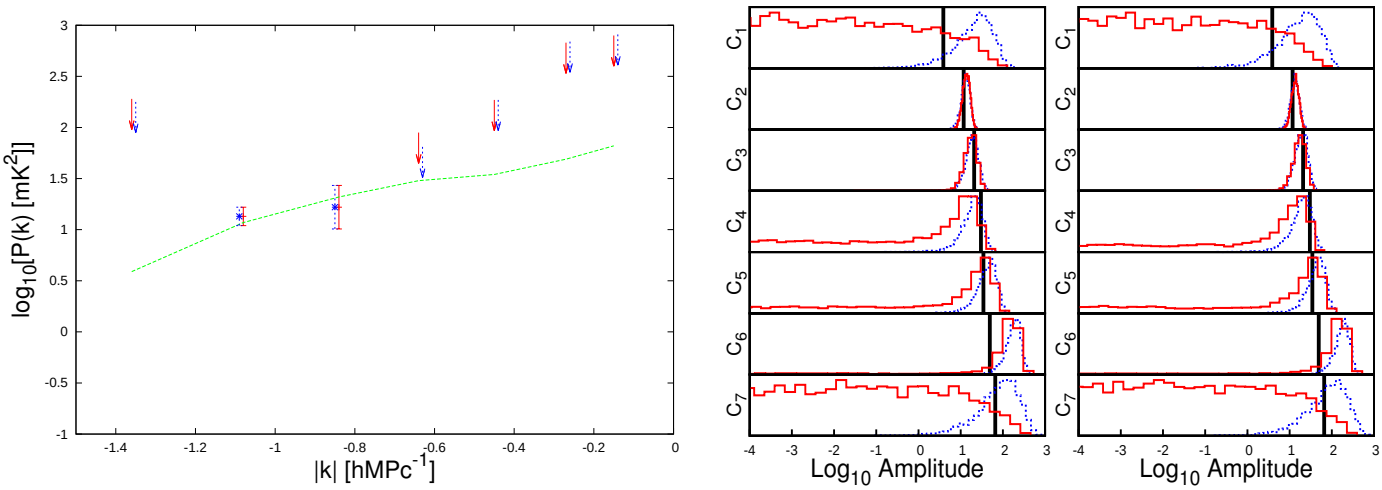

Figure 5. (Left) Injected (green line) and recovered values for the spherical power spectrum for Simulation 2 (blue points) and Simulation 3 (red points). Arrows represent 2 sigma upper limits obtained using a uniform prior on the amplitudes of the coefficients, while points with error bars are the parameter estimates and 1σ uncertainties for terms detected using the Log prior. (Middle) One dimensional marginalised posteriors for the 7 spherical power spectrum coefficients from Simulation 1 using priors that are uniform in the amplitude (blue lines) and uniform in the log of the amplitude (red lines). (Right) As for the Middle plot but for simulation 2.

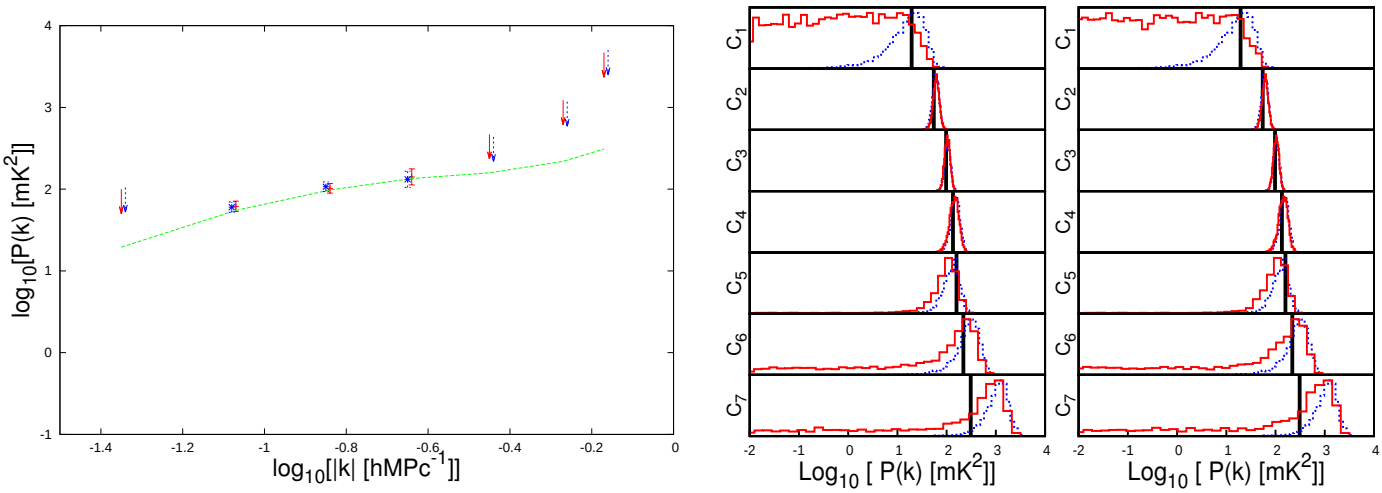

Figure 6. (Left) Injected (green line) and recovered values for the spherical power spectrum for Simulation 4 (blue points) and Simulation 5 (red points). Arrows represent 2 sigma upper limits obtained using a uniform prior on the amplitudes of the coefficients, while points with error bars are the parameter estimates and 1σ uncertainties for terms detected using the Log prior. (Middle) One dimensional marginalised posteriors for the 7 spherical power spectrum coefficients from Simulation 1 using priors that are uniform in the amplitude (blue lines) and uniform in the log of the amplitude (red lines). (Right) As for the Middle plot but for simulation 2.

6.3 Results for Simulations 4-5

Figure 6 shows the one dimensional marginalised posteriors for the spherical power spectrum coefficients from simulations 4 (middle plot) and 5 (right plot) when using priors that are uniform in the amplitude of the coefficient (blue line) and uniform in the log of the amplitude (red line). As we are now use the GHS to perform the sampling, we no longer obtain the evidence for different sets of coefficients. As such we consider a power spectrum coefficient 'detected' when the posterior is not consistent with $\log_{10}$ amplitudes less than -2 when using a logarithmic prior, which given the noise level in the simulation is equivalent to being consistent with zero. Compared to the 37 element array the 61 element array provides much greater constraints on the 2nd and 3rd spherical power spectrum coefficients, and provides a detection of the 4th coefficient. The remaining terms however are still consistent with zero when using logarithmic priors, and so we consider these only 2-σ upper limits, obtained using the uniform priors. All the coefficients for both simulations are consistent with the values obtained from the input cube within 2σ uncertainties.

7 CONCLUSIONS

We have presented a new Bayesian method for analysing interferometric data in order to estimate the three-dimensional power spectrum of density fluctuations in the neutral Hydrogen at the Epoch of Reionization.

We have described two applications of this method. i) Sampling directly from the power spectrum coefficients of the EoR signal by marginalising analytically over the signal coefficients, resulting in a compact parameter space (~ 10 dimensions) that requires large dense matrix inversions, and ii) sampling from the joint probability density of the power spectrum coefficients and the EoR signal realisation, resulting in large dimensionality (~ 20000 dimensions) but eliminating all matrix-matrix multiplications and costly matrix inversions from the likelihood calculation entirely, replacing them with matrix-vector operations and diagonal matrix inversions. In this case we performed the sampling process using a Guided Hamiltonian Sampler (B17) which provides an efficient means of sampling in large numbers of dimensions (potentially $> 10^6$).

We then used a series of simulations to show that both approaches presented allow for a reconstruction of the EoR power spectrum that is consistent with the model injected into the simulation in both high and low signal to noise regimes. When adding a simple, flat spectrum continuum model, the power in which was $\sim 10^8$ times greater than the EoR signal, we showed that the estimates of the power spectrum were unaffected despite no prior knowledge of the value or distribution of source amplitudes continuum in the continuum sky being used in the analysis.

In Sims et al. (2016) this approach has been used to estimate the three-dimensional power spectrum of interferometric data sets in the presence of astrophysically realistic foregrounds. Here it was found that these foregrounds contain power on all scales of interest, and that simultaneous estimation of both the EoR and foregrounds is important in order to obtain statistically robust estimates of the EoR power spectrum. Biased results, and thus biased astrophysical parameter estimates, will be obtained from methodologies that do not incorporate this covariance. Thus, methods such as those discussed in this work will be essential as we move towards the eventual detection of the EoR, and attempt to infer astrophysical conclusions about galaxy formation in the early Universe.

8 ACKNOWLEDGEMENTS

This work was performed using the Darwin Supercomputer of the University of Cambridge High Performance Computing Service (http://www.hpc.cam.ac.uk/), provided by Dell Inc. using Strategic Research Infrastructure Funding from the Higher Education Funding Council for England and funding from the Science and Technology Facilities Council. PMS is supported by the INFN IS PD51 Indark.

REFERENCES

Bonaldi A., Brown M. L., 2014, arXiv, arXiv:1409.5300
Bouwens R. J., et al., 2010, ApJ, 709, L133
Bowman J. D., Morales M. F., Hewitt J. N., 2009, ApJ, 695, 183
Contaldi C. R., Ferreira P. G., Magueijo J., Górski K. M., 2000, ApJ, 534, 25
Duane S., Kennedy A. D., Pendleton B. J., Roweth D., 1987, PhLB, 195, 216
Feroz F., Hobson M. P., Bridges M., 2009, MNRAS, 398, 1601
Feroz F., Hobson M. P., 2008, MNRAS, 384, 449
Gilbert J. & Lemarchal C., 1989, Mathematical Programming 45, pp. 407-435
Hamaker J. P., Bregman J. D., Sault R. J., 1996, A&AS, 117, 137
Harker G., et al., 2009, MNRAS, 397, 1138
Jelić V., et al., 2008, MNRAS, 389, 1319
Karakci A., Sutter P. M., Zhang L., Bunn E. F., Korotkov A., Timbie P., Tucker G. S., Wandelt B. D., 2013, ApJS, 204, 10
Kass R. E., Raftery A. E., 1995, Journal of the American Statistical Association, 90 (430): 791.
J. Kennedy & R. C. Eberhart, 1995, IEEE Int. Conf. Neural, Networks 4, 1942
J. Kennedy & R. C. Eberhart,2001,Swarm Intelligence, Morgan Kufmann, San Francisco
Lentati L., Alexander P., Hobson M. P., Taylor S., Gair J., Balan S. T., van Haasteren R., 2013, Phys. Rev. D, 87, 104021
Lentati L., Hobson M. P., Alexander P., 2014, MNRAS, 444, 3863
Lentati, L., Kerr, M., Dai, S., et al. 2016, arXiv:1612.05258
Loeb A., Furlanetto S. R., 2013, fgu..book,
Mellema G., et al., 2013, ExA, 36, 235
Mesinger A., Furlanetto S., Cen R., 2011, MNRAS, 411, 955
Mesinger A., Furlanetto S., 2007, ApJ, 669, 663
Morales M. F., Wyithe J. S. B., 2010, ARA&A, 48, 127
Neal R., 1993, Technical report, Probabilistic Inference Using MCMCM. Department of Computer Science, University of Toronto, Toronto

Neal R., 1996, Bayesian Learning for Neural Networks. Springer-Verlag, New York.
Paciga G., et al., 2013, MNRAS, 433, 639
Parsons A. R., et al., 2014, ApJ, 788, 106
Planck Collaboration, et al., 2014, A&A, 571, AA16
Prasad J., Souradeep T., 2012, Phys. Rev. D, 85, 123008
Pritchard J. R., Loeb A., 2012, RPPh, 75, 086901
Rocha G., Magueijo J., Hobson M., Lasenby A., 2001, Phys. Rev. D, 64, 063512
Schenker M. A., et al., 2013, ApJ, 768, 196
Shaver P. A., Windhorst R. A., Madau P., de Bruyn A. G., 1999, A&A, 345, 380
Sims, P. H., Lentati, L., Alexander, P., & Carilli, C. L. 2016, MNRAS, 462, 3069
Smirnov O. M., 2011, A&A, 527, AA106
Sutter P. M., Wandelt B. D., Malu S. S., 2012, ApJS, 202, 9
Sutter P. M., et al., 2014, MNRAS, 438, 768
Taylor J. F., Ashdown M. A. J., Hobson M. P., 2008, MNRAS, 389, 1284
Taylor G. B., Carilli C. L., Perley R. A., 1999, ASPC, 180,
Tingay S. J., et al., 2013, PASA, 30, e007
van Haarlem M. P., et al., 2013, A&A, 556, AA2
van Haasteren, R., & Levin, Y. 2013, MNRAS, 428, 1147